

See discussions, stats, and author profiles for this publication at:
<https://www.researchgate.net/publication/220206706>

A shock-capturing methodology based on adaptative spatial filtering for high-order non-linear computations

ARTICLE *in* JOURNAL OF COMPUTATIONAL PHYSICS · MARCH 2009

Impact Factor: 2.43 · DOI: 10.1016/j.jcp.2008.10.042 · Source: DBLP

CITATIONS

95

READS

124

3 AUTHORS, INCLUDING:

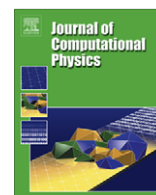


[Christophe Bailly](#)

Ecole Centrale de Lyon

231 PUBLICATIONS 3,675 CITATIONS

SEE PROFILE



A shock-capturing methodology based on adaptative spatial filtering for high-order non-linear computations

Christophe Bogey^{*,1}, Nicolas de Cacqueray², Christophe Bailly³

Laboratoire de Mécanique des Fluides et d'Acoustique, UMR CNRS 5509, Ecole Centrale de Lyon, 69134 Ecully Cedex, France

ARTICLE INFO

Article history:

Received 11 June 2008

Received in revised form 17 October 2008

Accepted 30 October 2008

Available online 17 November 2008

Keywords:

Shock-capturing

Finite differences

Spatial filtering

High-order

ABSTRACT

A shock-capturing methodology is developed for non-linear computations using low-dissipation schemes and centered finite differences. It consists in applying an adaptative second-order filtering to handle discontinuities in combination with a background selective filtering to remove grid-to-grid oscillations. The shock-capturing filtering is written in its conservative form, and its magnitude is determined dynamically from the flow solutions. A shock-detection procedure based on a Jameson-like shock sensor is derived so as to apply the shock-capturing filtering only around shocks. A second-order filter with reduced errors in the Fourier space with respect to the standard second-order filter is also designed. Linear and non-linear 1D and 2D problems are solved to show that the methodology is capable of capturing shocks without providing dissipation outside shocks. The shock detection allows in particular to distinguish shocks from linear waves, and from vortices when it is performed from dilatation rather than from pressure. Finally the methodology is simple to implement and reasonable in terms of computational cost.

© 2008 Elsevier Inc. All rights reserved.

1. Introduction

Issues [1] specific to computational aeroacoustics (CAA) have led over the last 15 years to the design of appropriate methods, reported for instance in the review of Colonius and Lele [2], which are less dispersive and less dissipative than standard methods of computational fluids dynamics (CFD). Centered differentiation schemes have in particular been considered to minimize numerical damping. They are however inaccurate for the higher wavenumbers discretized, and might generate numerical instabilities, specially for grid-to-grid oscillations, and therefore are usually implemented in combination with filtering of the high-frequency waves involving selective filters [3–7] affecting the low-frequency waves in a negligible manner. These methods have been applied successfully to compressible unsteady Navier–Stokes computations for predicting the noise generated by turbulent flows [2,8,9], and have moreover been shown to be well suited to perform accurate large-eddy simulations [10,11]. They can also be used for strongly non-linear problems, such as the generation of screech noise in supersonic jets as in Berland et al. [12], but it is generally recognized that they encounter serious problems for flows containing discontinuities such as shocks. Near shocks, the implementation of low-dissipation schemes might indeed result in spurious Gibbs oscillations due to spectral truncation in the wavenumber space.

* Corresponding author. Fax: +33 4 72 18 91 43.

E-mail addresses: christophe.bogey@ec-lyon.fr (C. Bogey), nicolas.cacqueray@ec-lyon.fr (N. de Cacqueray), christophe.bailly@ec-lyon.fr (C. Bailly).

¹ Research Scientist, CNRS.

² Ph.D. student.

³ Professor at Ecole Centrale de Lyon and Institut Universitaire de France.

In order to prevent the appearance of Gibbs oscillations in simulations of shocked flows, the usual approach is based on shock-capturing upwind-biased schemes. Such schemes have been formulated since the early eighties by many researchers including, among others, Harten et al. [13–18]. To handle shocks, these authors developed famous CFD algorithms such as the TVD (total variation diminishing) schemes making use of flux or slope limiters, and the ENO (essentially non-oscillatory) and WENO (weighted ENO) schemes in which an adaptive stencil that adjusts to the smoothness of the solutions is applied, refer for instance to the two reviews made by Shu [19] and Pirozzoli [20] for more details. These schemes ensure high stability, but they are in general of low accuracy, especially for time-dependent problems. They might provide unsatisfactory results for shock–turbulence interaction problems [21], as well as excessive numerical damping on turbulent scales in large-eddy simulations [22]. Attempts have therefore been made to improve their performance by modifying their design [23] or by increasing their formal order [24]. In this case, in order to assess the quality of the solutions, in particular in aeroacoustic studies, there is an urgent need of analysing the spectral properties of the shock-capturing schemes in the Fourier space [25], and of checking their accuracy by solving standard CAA test cases [26,27]. Another interesting approach suggested by Adams and Shariff [28] is to couple compact/low-dissipation schemes with a shock-capturing scheme that is turned on around discontinuities [28–30]. The adaptation of the spatial scheme then requires the detection of the strong non-linear features within the computational domain. This has been done for instance by Visbal and Gaitonde [31] who applied a shock detector to switch between compact and shock-capturing schemes, but furthermore explored a different methodology where numerical filtering is adapted to the flow features.

With the aim of using centered differentiation schemes to keep good resolution characteristics, one possibility is indeed to make use of an adaptive artificial dissipation model, corresponding also to a filtering of the solutions, which is effective near the discontinuities but tends to have negligible influence everywhere else. Jameson et al. [32] thus introduced additional terms in the Euler equations that consist of a blend of second-order and fourth-order dissipations with non-linear switching coefficients. Their method was applied by Pulliam [33] and Swanson and Turkel [34] for steady inviscid flows around airfoils, but it was found to be too dissipative for unsteady problems. For aeroacoustics purposes, Lockard and Morris [35] and Kim and Lee [36] proposed higher-order versions of Jameson's model, in which the selective dissipation of Tam et al. [4,5] is implemented rather than the original fourth-order dissipation. Similarly Visbal and Gaitonde [31], Hixon et al. [37] and Emmert et al. [38] recently developed shock-capturing dissipation models combining second-order and high-order diffusion operators. One crucial point in the methodology is the definition of the shock detector, which has to distinguish between shocks and gradients of any other kind in order to limit the range of the shock-capturing dissipation specifically to the regions containing shocks [39]. Detectors estimated from simple gradients [28,30], from second derivatives of pressure or density [32,36–38] such as the Jameson detector, and from WENO-type smoothness criteria [31,40] have in particular been used. Ducros et al. [41] also proposed a modified version of the Jameson detector taking into account the local property of compressibility, which is capable of discriminating between turbulent fluctuations and shocks [40,42]. Finally, once the shock-detection sensor is evaluated, the shock region is dealt with by means of a switch which has to specify the type and amount of dissipation to be specified at each grid point.

In the present study, a shock-capturing methodology based on an adaptive spatial filtering is derived for high-accuracy non-linear computations including low-dissipation time integration and centered space differencing. Following the works presented above, it consists in applying a background selective filtering at each mesh point to remove grid-to-grid oscillations, in combination with a shock-capturing filtering around discontinuities. To smooth possible shocks in a proper manner, the shock-capturing filtering is written in a conservative form and is of second-order, but its magnitude has to be adjusted dynamically from the flow solutions to be nil in regions of linear propagation, for well-resolved gradients and for turbulent fluctuations, so that the approach should be appropriate for unsteady CAA and CFD problems. To meet this requirement, a second-order filter reducing phase errors with respect to the standard second-order filter when applied with a non-uniform strength is first designed. A Jameson-like shock sensor evaluated from the magnitude of the higher wavenumbers of the flow variables is then proposed. It can be estimated either from pressure as classically done, or from dilatation in order to give weight to the local feature of compressibility in the procedure of shock detection. The magnitude of the shock-capturing filtering is finally determined from the shock sensor in a simple way, using a given threshold parameter. The efficiency of the shock-capturing methodology is assessed by solving standard linear and non-linear problems [43,44,49,50] with a low-dissipation Runge–Kutta algorithm and centered finite differences, built up in Bogey and Bailly [7] to be well suited to CAA needs. Problems of acoustic wave and shock propagation, vortex convection, shock–sound interaction, shock tubes and shock–vortex interaction are specially considered. The influence of some methodology parameters such as the filter shape, the use of pressure or dilatation for detecting the shock, and the threshold parameter providing the filtering strength is thus discussed, in order to draw recommendations. The application of the selective filtering to the fluxes [51] rather than to the flow variables is also briefly discussed for a non-linear problem.

The present paper is organized as follows: the equations governing the test problems and the background numerical algorithm, including a sixth-order selective filter, are reported in Section 2. The development of the shock-capturing filtering procedure is detailed in Section 3, with a focus on the impact of the conservative form of the filtering in the Fourier space, the definition of the shock detector and the determination of the filtering magnitude. The results obtained for the test cases using the adaptive shock-capturing filtering are then shown in Section 4. Concluding remarks are finally provided in Section 5.

2. Equations and numerical algorithm

2.1. Governing equations

To quantify the effects of the shock-capturing filtering on the behaviour and interactions of different kinds of disturbances, solutions of test cases will be calculated in Section 4 by solving problems of acoustic and shock propagation, vortex convection, shock–sound interaction in a transonic nozzle, shock tubes and shock–vortex interaction. They will be computed from the one-dimensional, the quasi-one-dimensional or the two-dimensional Euler equations written in a conservative form using Cartesian coordinates. Dimensionless variables defined by introducing reference scales for density, length and velocity (sound speed) are used.

2.1.1. One-dimensional equations

The one-dimensional Euler equations are expressed in the form

$$\frac{\partial U}{\partial t} + \frac{\partial E}{\partial x} = 0, \quad (1)$$

where the vector U of conservative variables and the flux vector E are defined as $U = [\rho, \rho u, \rho e]^T$ and $E = [\rho u, \rho u^2 + p, u(\rho e + p)]^T$, and ρ , u , p denote density, velocity and pressure. The total energy is given by $\rho e = p/(\gamma - 1) + \rho u^2/2$ with $\gamma = 1.4$.

2.1.2. Quasi-one-dimensional equations

The quasi-one-dimensional Euler equations are written in the form

$$\frac{\partial U}{\partial t} + \frac{\partial E}{\partial x} + Q = 0, \quad (2)$$

where the variable vector U , the flux vector E and the source vector Q are respectively given by $U = [\rho, \rho u, \rho e]^T$, $E = [\rho u, \rho u^2 + p, u(\rho e + p)]^T$ and $Q = (1/A)(dA/dx)[\rho u, \rho u^2, u(\rho e + p)]^T$, and $A = A(x)$ is the cross-sectional area.

2.1.3. Two-dimensional equations

The two-dimensional Euler equations are finally expressed as

$$\frac{\partial U}{\partial t} + \frac{\partial E}{\partial x} + \frac{\partial F}{\partial y} = 0, \quad (3)$$

where the variable vector U and the flux vectors E and F are provided by $U = [\rho, \rho u, \rho v, \rho e]^T$, $E = [\rho u, \rho u^2 + p, \rho u v, u(\rho e + p)]^T$ and $F = [\rho v, \rho u v, \rho v^2 + p, v(\rho e + p)]^T$. The total energy is now given by $\rho e = p/(\gamma - 1) + \rho(u^2 + v^2)/2$, where u and v are the two velocity components.

2.2. Numerical algorithm

When Eqs. (1)–(3) are solved, the spatial derivatives are approximated with 11-point fourth-order centered finite differences, which have been designed [7] so as to generate negligible phase errors down to waves discretized by four points per wavelength. Time integration is performed using a six-stage second-order low-storage Runge–Kutta algorithm displaying low-dispersion and low-dissipation in the Fourier space [7]. These methods have been successfully implemented in previous studies to perform direct noise computations for configurations such as subsonic and supersonic jets [12,52,53], and flows around an airfoil [54].

During the computations, a background numerical dissipation is applied in the following way: after each time step, the conservative variables U are filtered explicitly using an 11-point selective filter at a magnitude σ^f , to provide at node i

$$U_i^{sf} = U_i - \sigma^f D_i^f, \quad (4)$$

where $0 \leq \sigma^f \leq 1$, and the filtering operator is given by

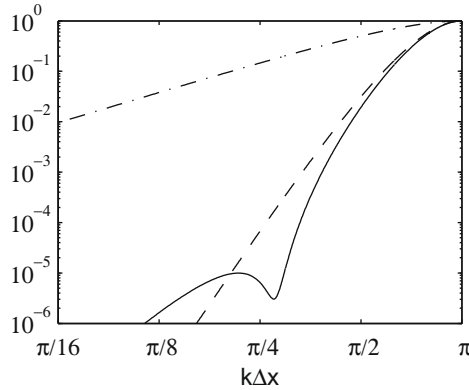
$$D_i^f = \sum_{j=-5}^5 d_j U_{i+j} \quad (5)$$

and d_j are the filter coefficients. The filtering procedure is conservative as long as a constant magnitude σ^f is used. In what follows, this magnitude is moreover set to $\sigma^f = 1$, implying that grid-to-grid oscillations are completely removed after each time iteration.

The selective filter involved in the present study is an 11-point sixth-order filter, whose coefficients d_j , reported in Table 1, have been determined so that its damping function $D_k(k\Delta x) = d_0 + 2\sum_{j=1}^5 d_j \cos(jk\Delta x)$ is lower than 10^{-5} over a large wave-number range.

Table 1Coefficients of the 11-point sixth-order selective filter, with $d_{-j} = d_j$.

$d_0 = 0.234810479761700$
$d_1 = -0.199250131285813$
$d_2 = 0.120198310245186$
$d_3 = -0.049303775636020$
$d_4 = 0.012396449873964$
$d_5 = -0.001446093078167$

**Fig. 1.** Damping function, in logarithmic scales, as a function of the wavenumber $k\Delta x$: — optimized 11-point filter of order 6, --- standard 10th-order filter, standard second-order filter.

The damping function thus obtained is shown in Fig. 1. Compared to the standard second-order filter, i.e. to a typical shock-capturing filter, the selective filter differs basically by providing appreciable dissipation only for waves roughly over $\pi/2 \leq k\Delta x \leq \pi$, discretized by fewer than four grid points, whereas the second-order filter might affect small wavenumbers. To evaluate accuracy limits of the selective filter, the two criteria $D_k(k\Delta x) \leq 2.5 \times 10^{-3}$ and $D_k(k\Delta x) \leq 2.5 \times 10^{-4}$ are used as previously in Bogey and Bailly [7], yielding $\lambda/\Delta x = 4.82$ and $\lambda/\Delta x = 5.74$ in terms of number of points per wavelength. These limits are lower for instance than the limits $\lambda/\Delta x = 5.40$ and $\lambda/\Delta x = 6.96$ found for the standard 10th-order filter also represented in Fig. 1.

Finally, boundary conditions based on characteristics [56] are implemented in the quasi-one-dimensional problems, whereas the non-radiation boundary conditions derived by Tam and Dong [55] are applied in the two-dimensional cases.

3. Shock-capturing filtering

The aim is to develop a shock-capturing filtering procedure appropriate for unsteady high-order simulations. Therefore the filtering will be of second-order, and written in a conservative form to accurately describe the propagation of shocks, and its magnitude will have to be adjusted dynamically from the flow variables so that it is negligible everywhere except around discontinuities.

3.1. Conservative form of the filtering

The shock-capturing filtering is applied at each time step just after the background selective filtering removing grid-to-grid oscillations. Since its magnitude depending on the shock detection is expected to vary, the filtering operation is written in a conservative form as the difference between two damping fluxes taken at the interface of two adjacent cells as recommended by Kim and Lee [36]. At point i on an uniform grid, the conservative variables U are thus filtered explicitly to yield

$$U_i^{\text{sc}} = U_i - \left(\sigma_{i+\frac{1}{2}}^{\text{sc}} D_{i+\frac{1}{2}}^{\text{sc}} - \sigma_{i-\frac{1}{2}}^{\text{sc}} D_{i-\frac{1}{2}}^{\text{sc}} \right), \quad (6)$$

where the filtering strength $0 \leq \sigma^{\text{sc}} \leq 1$ is not constant, and the damping functions $D_{i+\frac{1}{2}}^{\text{sc}}$ and $D_{i-\frac{1}{2}}^{\text{sc}}$ are estimated from the variables U using the following interpolations:

$$D_{i+\frac{1}{2}}^{\text{sc}} = \sum_{j=1-n}^n c_j U_{i+j} \quad \text{and} \quad D_{i-\frac{1}{2}}^{\text{sc}} = \sum_{j=1-n}^n c_j U_{i+j-1} \quad (7)$$

To determine the coefficients c_j of the $2n$ -point interpolation defining the damping functions, one considers the non-conservative form of the filtering

$$U_i^{sc} = U_i - \sigma_i^{sc} \sum_{j=-n}^n d_j U_{i+j} \quad (8)$$

and notes that Eqs. (6) and (8) must be equivalent when the filtering magnitude is uniform. For a given n , the coefficients c_j are then directly obtained from the coefficients d_j of the corresponding non-conservative centered filter. The values found for the standard second-order filter, here referred to as Fo2, are collected in Table 2. The coefficients c_j calculated for the standard fourth-order filter Fo4 are also given in the table, despite this filtering is not dissipative enough to handle strong discontinuities in a proper manner and will not be used to capture shocks subsequently.

3.2. Characteristics of the filtering in the Fourier space

The effects of the shock-capturing filtering are investigated in the Fourier space by considering the application of the conservative form (6) of the filtering with a non-uniform magnitude $\sigma_{i+\frac{1}{2}}^{sc} = \sigma_i^{sc} + \Delta\sigma_i^{sc}$ and $\sigma_{i-\frac{1}{2}}^{sc} = \sigma_i^{sc} - \Delta\sigma_i^{sc}$ (by construction $0 \leq \sigma_i^{sc} \leq 1$ and $-0.5 \leq \Delta\sigma_i^{sc} \leq 0.5$), yielding

$$U_i^{sc} = U_i - \sigma_i^{sc} (D_{i+\frac{1}{2}}^{sc} - D_{i-\frac{1}{2}}^{sc}) - \Delta\sigma_i^{sc} (D_{i+\frac{1}{2}}^{sc} + D_{i-\frac{1}{2}}^{sc}). \quad (9)$$

Introducing the damping functions (7) into expression (9) provides

$$U_i^{sc} = U_i - \sigma_i^{sc} \left\{ c_n U_{i+n} + \sum_{j=1}^{n-1} (c_j - c_{j+1}) U_{i+j} - c_{1-n} U_{i-n} \right\} - \Delta\sigma_i^{sc} \left\{ c_n U_{i+n} + \sum_{j=1}^{n-1} (c_j + c_{j+1}) U_{i+j} + c_{1-n} U_{i-n} \right\} \quad (10)$$

In order that the second term in the right-hand side of Eq. (10) should be equivalent to a filtering at the magnitude σ_i^{sc} providing no dispersion, that is a filtering based on symmetrical coefficients, one has to set $c_n = -c_{1-n}$ and $c_j - c_{j+1} = c_{-j} - c_{1-j}$. The coefficients of the damping functions are then antisymmetric with $c_j = -c_{1-j}$, and the filtering procedure (10) becomes

$$U_i^{sc} = U_i - \sigma_i^{sc} \left\{ -2c_1 U_i + \sum_{j=1}^{n-1} (c_j - c_{j+1}) (U_{i+j} + U_{i-j}) + c_n (U_{i+n} + U_{i-n}) \right\} - \Delta\sigma_i^{sc} \left\{ \sum_{j=1}^{n-1} (c_j + c_{j+1}) (U_{i+j} - U_{i-j}) + c_n (U_{i+n} - U_{i-n}) \right\} \quad (11)$$

Applying spatial Fourier transform to Eq. (11) allows us to write

$$\widehat{U_i^{sc}} = \widehat{U_i} (1 - \sigma_i^{sc} D_{real}(k\Delta x) + i\Delta\sigma_i^{sc} D_{imag}(k\Delta x)), \quad (12)$$

where $D_{real}(k\Delta x)$ is the transfer function of the equivalent filter obtained with a uniform filtering magnitude, and $D_{imag}(k\Delta x)$ is the transfer function of the phase errors generated by the variations of the filtering strength. They are defined by

$$D_{real}(k\Delta x) = -2c_1 + 2 \sum_{j=1}^{n-1} (c_j - c_{j+1}) \cos(jk\Delta x) + 2c_n \cos(nk\Delta x), \quad (13)$$

$$\text{and } D_{imag}(k\Delta x) = -2 \sum_{j=1}^{n-1} (c_j + c_{j+1}) \sin(jk\Delta x) - 2c_n \sin(nk\Delta x). \quad (14)$$

The transfer functions for the standard second- and fourth-order filters Fo2 and Fo4 are presented in Fig. 2. The profiles for $D_{real}(k\Delta x)$ in Fig. 2(a) correspond to the damping functions classically observed as a function of the wavenumber, with the decrease of dissipation as the order increases. Those for $D_{imag}(k\Delta x)$ in Fig. 2(b) suggest that the phase errors might be important for the second-order filter.

An attempt is now made to develop a specific 4-point conservative filter for shock-capturing, referred to as Fopt, that displays dissipation features similar to those of the standard second-order filter Fo2, but also generates reduced errors. The filter is then designed so that its damping function $D_{real}(k\Delta x)$ approximates the damping function $D_{real}^{Fo2}(k\Delta x)$ of filter Fo2, while lowering its related phase errors given by $D_{imag}(k\Delta x)$ for a given range of wavenumbers. In practice the coefficients c_j of the filter Fopt are chosen so that the integral error

Table 2

Coefficients c_j for conservative shock-capturing filtering: standard second-order filter (Fo2), standard fourth-order filter (Fo4), and optimized second-order filter (Fopt), with $c_{1-j} = -c_j$.

	Fo2	Fo4	Fopt
c_1	$-1/4$	$-3/16$	-0.210383
c_2	0	$1/16$	0.039617

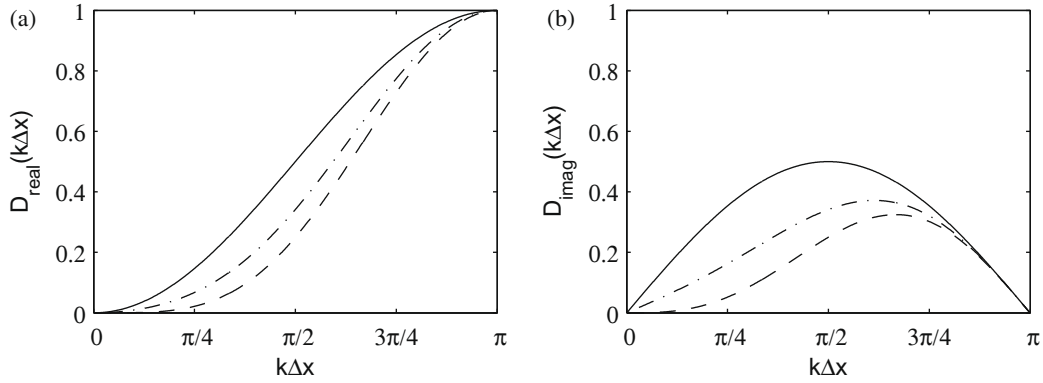


Fig. 2. Transfer functions, as a function of the wavenumber, of the real and imaginary parts, (a) $D_{\text{real}}(k\Delta x)$ and (b) $D_{\text{imag}}(k\Delta x)$, for conservative shock-capturing filtering: — standard second-order filter (Fo2), --- standard fourth-order filter (Fo4), and -.-.- optimized second-order filter (Fopt).

$$\int_0^\pi [D_{\text{real}}(k\Delta x) - D_{\text{real}}^{\text{Fo2}}(k\Delta x)]^2 d(k\Delta x) + \int_0^{\frac{2\pi}{5}} [D_{\text{imag}}(k\Delta x)]^2 d(k\Delta x) \quad (15)$$

is minimized. The optimization is carried out by imposing $0 \leq D_r \leq 1$ for $0 \leq k\Delta x \leq \pi$. Two regularization constraints must also be satisfied: $D_r(k\Delta x = 0) = 0$, which is naturally ensured by expression (13), and $D_r(k\Delta x = \pi) = 1$ yielding

$$c_1 = -\frac{1}{4} + \sum_{j=2}^n (-1)^j c_j. \quad (16)$$

Therefore, for a 4-point filter defined by antisymmetric coefficients, there is only one coefficient to adjust.

The coefficients of the filter Fopt are reported in Table 2, and the corresponding transfer functions are presented in Fig. 2. Compared to the filter Fo2, the optimized filter shows phase errors decreased by a factor of about 2 for small wavenumbers, while being significantly more dissipative than the filter Fo4. Its shock-capturing capabilities will be discussed in Section 4 devoted to the test cases.

3.3. Adaptive filtering magnitude

The filtering strength σ^{sc} is to be estimated from the flow variables, so that it should be significant around discontinuities but negligible everywhere else. A procedure of shock detection is therefore first proposed. More precisely, in order to indicate the presence of shocks within the computational domain, a shock detector, roughly similar to that formulated by Jameson et al. [32] making use of the second derivative of pressure, is evaluated from the magnitude of the high-wavenumber components of a variable that can be either pressure or dilatation.

Based on pressure, the present shock sensor is determined following three steps. The pressure high-wavenumber components are first extracted from variable p using the second-order filter Fo2, yielding, at node i

$$Dp_i = (-p_{i+1} + 2p_i - p_{i-1})/4. \quad (17)$$

The magnitude of the high-pass filtered pressure is then calculated as

$$Dp_i^{\text{magn}} = \frac{1}{2} [(Dp_i - Dp_{i+1})^2 + (Dp_i - Dp_{i-1})^2] \quad (18)$$

and the shock sensor is defined as the ratio r expressed as

$$r_i = \frac{Dp_i^{\text{magn}}}{p_i^2} + \epsilon, \quad (19)$$

where $\epsilon = 10^{-16}$ is introduced to avoid numerical divergence later in expression (23).

In some cases the use of pressure to detect shocks might not be appropriate for distinguishing between turbulent fluctuations and shocks in an unambiguous manner. To deal with this deficiency, as also suggested by Ducros et al. [41], a possibility is to take into account the local property of compressibility. This led us to perform the shock detection from dilatation $\Theta = \nabla \cdot \mathbf{u}$ rather than from pressure. The high-pass filtered dilatation is computed at node i as

$$D\Theta_i = (-\Theta_{i+1} + 2\Theta_i - \Theta_{i-1})/4 \quad (20)$$

and its amplitude as

$$D\Theta_i^{magn} = \frac{1}{2} \left[(D\Theta_i - D\Theta_{i+1})^2 + (D\Theta_i - D\Theta_{i-1})^2 \right]. \quad (21)$$

The shock sensor based on dilatation is then calculated as

$$r_i = \frac{D\Theta_i^{magn}}{c_i^2 / \Delta x^2} + \epsilon, \quad (22)$$

where $c_i^2 = \gamma p_i / \rho_i$ is the square of the local sound speed.

Once the value of the shock detector r is known, from pressure or dilatation, the strength of the filtering has to be given. In the present approach, following Visbal and Gaitonde [31] for instance, a threshold parameter r_{th} is used to specify the regions where the shock-capturing filtering is employed. The filtering magnitude is evaluated by the function

$$\sigma_i^{sc} = \frac{1}{2} \left(1 - \frac{r_{th}}{r_i} + \left| 1 - \frac{r_{th}}{r_i} \right| \right) \quad (23)$$

which is represented in Fig. 3. For $r_i \leq r_{th}$, the filtering magnitude is $\sigma_i^{sc} = 0$ as required. For $r_i > r_{th}$, that is when the level of the high-wavenumber components of pressure or dilatation are appreciable, one gets $0 < \sigma_i^{sc} < 1$, and in particular $\sigma_i^{sc} \rightarrow 1$ for $r_i \rightarrow +\infty$. In this way, the second-order filter is only switched on when the gradients of pressure or dilatation are strong enough. The threshold parameter r_{th} is typically to be set between 10^{-6} and 10^{-4} , a lower value corresponding to an application of the shock-capturing filtering on a wider region, leading to smoother solutions. A threshold value of $r_{th} = 10^{-5}$ will be in addition shown later to provide appropriate results for the different test problems solved, and could be recommended as a reference parameter.

For completeness, for the application of the conservative form (6) of the shock-capturing filtering, the values of σ^{sc} between the nodes are simply approximated by

$$\sigma_{i+\frac{1}{2}}^{sc} = \frac{1}{2} (\sigma_{i+1}^{sc} + \sigma_i^{sc}) \quad \text{and} \quad \sigma_{i-\frac{1}{2}}^{sc} = \frac{1}{2} (\sigma_i^{sc} + \sigma_{i-1}^{sc}). \quad (24)$$

4. Test cases

Two kinds of test problems are solved to study the relevance and the efficiency of the shock-capturing methodology. First linear problems (acoustic propagation and vortex convection) are considered in order to verify that the shock-capturing filtering does not apply in these cases. Then non-linear problems involving shocks (shock propagation, shock–acoustic interactions, shock tubes and shock–vortex interactions) are simulated to demonstrate the capability of the methodology to take into account discontinuities in a proper manner. As previously mentioned, the numerical algorithm used for the discretization of the test cases combines 11-point low-dispersion centered finite differences with a 6-stage optimized Runge–Kutta schemes designed in Bogey and Bailly [7], and a background selective filtering of the conservative variables is implemented after each time step using the 11-point filter of sixth-order presented in Section 2.2, with a magnitude $\sigma^{sf} = 1$.

4.1. Linear problems

Two test cases are first computed in order to check whether the shock-capturing filtering is turned on in linear problems involving acoustical or vortical disturbances.

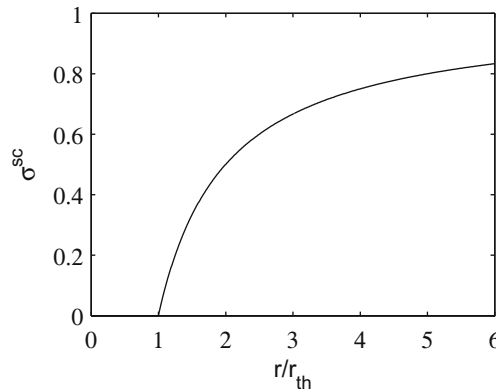


Fig. 3. Variations of the shock-capturing filtering magnitude σ^{sc} as a function of the shock sensor r/r_{th} .

4.1.1. Acoustic propagation

In order to compute the propagation of an acoustic wave from the one-dimensional Euler equations (1), with or without making use of the shock-capturing procedure, a pressure pulse is specified by imposing at time $t = 0$ the following conditions:

$$u = 0, \quad p = \frac{1}{\gamma} \left(1 + 0.0002 \exp \left[-\ln(2) \left(\frac{x}{b} \right)^2 \right] \right) \quad \text{and} \quad \rho = 1,$$

where b is the Gaussian half-width of the pulse. The pressure amplitude of the right-going travelling wave generated by the initial pulse is 10^4 times smaller than the ambient pressure $1/\gamma$, so that non-linear effects are negligible during the propagation. The problem is solved on a uniform grid with a mesh spacing $\Delta x = 1$, with a time step $\Delta t = 0.8$.

To explore the adaptability of the shock-capturing method to linear wave propagation, two pulses, one well-resolved by the grid and another slightly under-resolved, defined respectively by half-widths $b = 2$ and $b = 3$ are dealt with. The pressure profiles thus obtained at $t = 200$ without shock-capturing are presented in Fig. 4(a). There is no visible dispersion nor dissipation of the broader pulse with $b = 3$, whereas the shape of the pulse with $b = 2$ has been modified during the propagation with an amplitude that has been in particular noticeably decreased by the selective filtering. The pressure profiles determined when the shock-capturing procedure is switched on are not represented here, but they collapse perfectly with the previous profiles for both pulse configurations. The shock detectors r calculated at $t = 200$ from pressure or from dilatation are indeed shown in Fig. 4(b) and (c) to be lower than 10^{-10} . These values are well below the threshold parameter which is typically between $r_{th} = 10^{-6}$ and $r_{th} = 10^{-4}$. Consequently the magnitude of the shock-capturing filtering is set to $\sigma^{sc} = 0$, and the shock-capturing filtering is not employed in the present linear problems.

4.1.2. Vortex convection

The convection of a round vortex by a uniform flow is now considered by solving the two-dimensional Euler equations (3). At $t = 0$, the following initial conditions are then imposed:

$$u = 0.5 - \frac{y}{b} \exp \left[-\ln(2) \left(\frac{x^2 + y^2}{b^2} \right) \right], \quad v = \frac{x}{b} \exp \left[-\ln(2) \left(\frac{x^2 + y^2}{b^2} \right) \right], \quad p = \frac{1}{\gamma}, \quad \text{and} \quad \rho = 1$$

in order to introduce a divergence-free vortex at $x = y = 0$, similarly to what was done in the first CAA Workshop [43], which will be convected in the axial direction at the dimensionless velocity 0.5 that is half the speed of sound. The computation is performed on a grid containing 181×121 points with mesh spacings $\Delta x = \Delta y = 1$, with a time step $\Delta t = 0.5$. When the shock-capturing procedure is applied, the standard second-order filter Fo2 is used in its conservative form, and a threshold parameter $r_{th} = 10^{-4}$ is specified for the shock detector. In addition, as previously for the acoustic pulses, two geometrical configurations are studied: a well-resolved vortex defined by a Gaussian half-width $b = 5$, and a vortex with $b = 3$ characterized by a narrower core.

As illustrations of the problem solutions, the vorticity and the pressure fields calculated at $t = 50$ for the vortex with $b = 5$ without shock-capturing are represented in Fig. 5. As expected, the vortex has been convected by the axial flow so as to be located at $x = 25$ and $y = 0$ in Fig. 5(a). A region with negative pressure induced by the vortex is also observed at this place in Fig. 5(b), while a transitory circular sound wave is noticed all around the vortical structure.

To give evidence of possible effects of the shock-capturing method on the present vortices, the pressure profiles obtained along $y = 0$ at time $t = 50$ with or without shock-capturing are shown in Fig. 6. They display pressure fluctuations of aerodynamic nature centered on the vortex core at $x = 25$, and acoustic pressure waves at $x = -30$ and $x = 80$. With respect to the solutions computed without shock-capturing in Fig. 6(a), the shock-capturing procedure using pressure as variable for the shock detection appears to damp the solutions in Fig. 6(b), especially for the narrower vortex with $b = 3$. Similar alterations due to shock-capturing are however not observed in Fig. 6(c), when dilatation rather than pressure is used to evaluate the shock sensor.

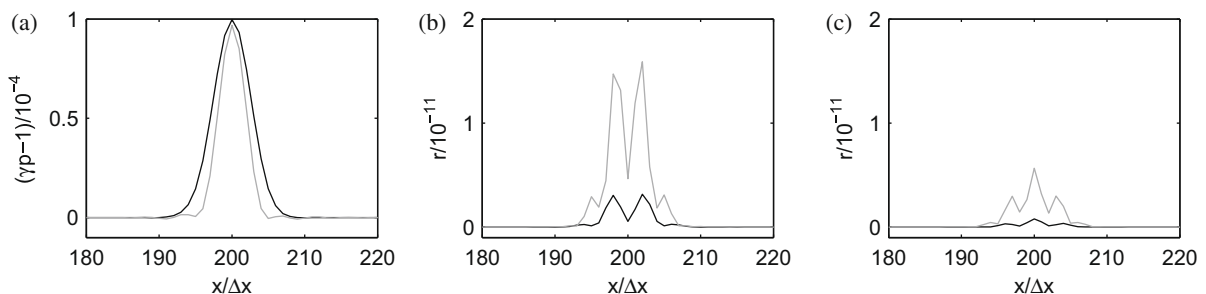


Fig. 4. Linear acoustic propagation. Solutions at $t = 200$: (a) pressure computed without using the shock-capturing procedure and, shock sensor r evaluated (b) from pressure and (c) from dilatation using the shock-capturing procedure. Gaussian pulse half-width: — $b = 3$, - - $b = 2$.

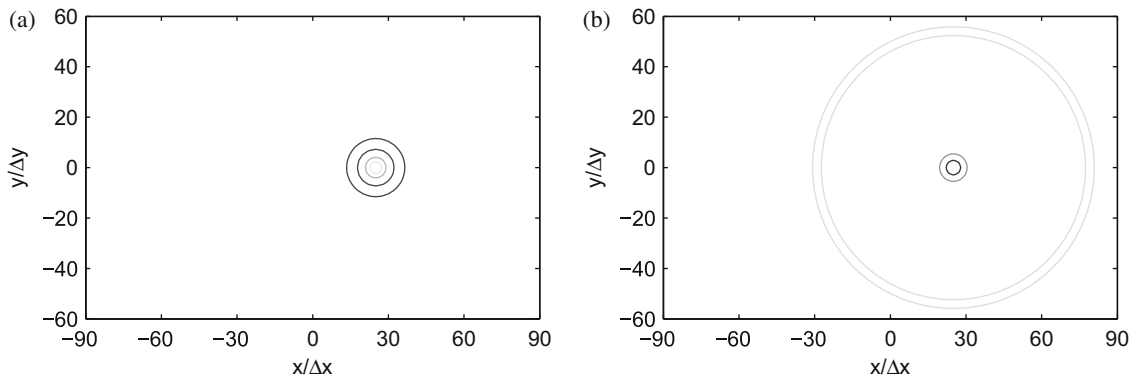


Fig. 5. Vortex convection. Solutions at $t = 50$ for the vortex with Gaussian half-width $b = 5$: (a) vorticity and (b) pressure, computed without using the shock-capturing procedure. Representation of contours: $\omega = [-0.03, 0.15, 0.25]$ for vorticity and $\gamma p = 1 + [-0.25, -0.1, 0.03]$ for pressure.

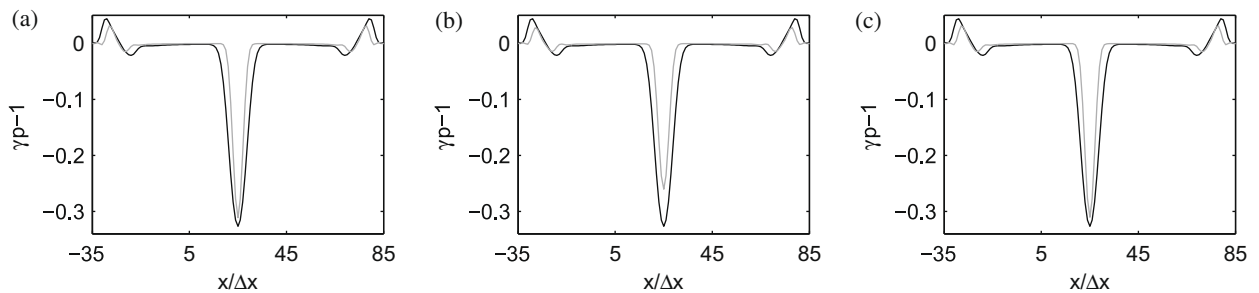


Fig. 6. Vortex convection. Profiles of pressure computed at $t = 50$ along $y = 0$: (a) without using the shock-capturing procedure, and using the shock-capturing procedure with a shock detector evaluated from (b) pressure and (c) dilatation. Gaussian half-width: — $b = 5$, — $b = 3$.

The discrepancies between the solutions obtained using the shock-capturing method in Fig. 6(b) and (c) result from the choice of variable involved in the estimation of the shock sensor. In the first case, pressure is used, yielding at $t = 50$ for the axial shock sensor r the profiles plotted in Fig. 7(a). Because of the important gradients of aerodynamic pressure around the vortices, the shock sensor is of significant magnitude at $x \simeq 25$. In this way it might indicate the presence of a shock and lead to the application of the shock-capturing filtering in the vortex region. In the present problems, the second-order filter has been in particular turned on in the beginning of the calculations, but is no more active at $t = 50$ because the threshold parameter is $r_{th} = 10^{-4}$. A different behaviour is found when dilatation is used to evaluate the shock sensor r . In this case, the shock sensor takes very small values around the vortices, as demonstrated by the profiles of Fig. 7(b), and the shock-capturing filtering does not apply. The use of dilatation in the procedure of shock detection therefore appears more appropriate in vortical flows because, contrary to pressure, it allows to distinguish a vortex from a shock.

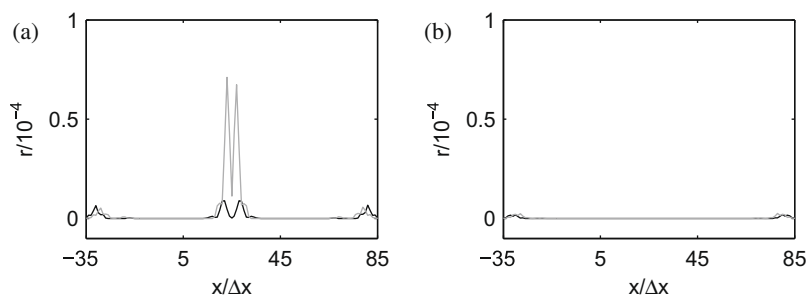


Fig. 7. Vortex convection. Profiles of the axial shock sensor r computed at $t = 50$ along $y = 0$: (a) from pressure, (b) from dilatation, using the shock-capturing procedure. Gaussian half-width: — $b = 5$, — $b = 3$.

4.2. Non-linear problems

Test cases are now simulated to look into the capability of the methodology to properly capture shocks without appreciably affecting the accuracy of the solutions on both sides of the shocks, especially when the shocks interact with acoustic or aerodynamic perturbations.

4.2.1. Shock propagation

The first non-linear problem studied is concerned with shock propagation. The test case is taken from the first CAA Workshop [43]. It is problem 2 from category 2, that is defined by the following initial perturbations at time $t = 0$:

$$u = 0.5 \exp \left[-\ln(2) \left(\frac{x}{5} \right)^2 \right], \quad p = \frac{1}{\gamma} \left(1 + \frac{\gamma-1}{2} u \right)^{\frac{2\gamma}{\gamma-1}} \quad \text{and} \quad \rho = \left(1 + \frac{\gamma-1}{2} u \right)^{\frac{2}{\gamma-1}}.$$

The problem is solved from the one-dimensional Euler equations (1), using a mesh grid of spacing $\Delta x = 1$ and a time step $\Delta t = 0.8$, to provide pressure distributions at $t = 200$.

Solutions are first computed without shock-capturing, by only applying selective filtering to the variables or to the fluxes. They are presented respectively in Fig. 8(a) and (b). In the first case, the initial Gaussian pulse has become triangular in shape due to non-linear effects. A shock is visible at $x \simeq 248\Delta x$, surrounded by high-frequency Gibbs oscillations indicative of the spectral truncation of pressure components. In the second case, the pressure pulse has been dispersed, and does not display a satisfactory shape. The numerical approach consisting in filtering the fluxes, previously shown to generate phase errors for linear equations [51], might therefore be not suitable for strongly non-linear problems.

In what follows, the background selective filtering is then applied to the conservative variables as described earlier in the paper, in combination with the shock-capturing method. Results obtained by varying the shock-capturing parameters are reported to assess the performance of the methodology.

The pressure profile determined using the non-conservative form of the shock-capturing filtering, with a shock detector evaluated from pressure, a threshold value $r_{th} = 10^{-5}$ and the filter Fo2, is presented in Fig. 8(c). The spurious Gibbs oscillations occurring without shock-capturing have been removed. However the shock is now located at $x \simeq 252\Delta x$, farther downstream in the axial direction. This illustrates that the conservative form of the shock-capturing filtering is required to properly calculate the speed of the shock propagation. The solutions shown subsequently are therefore all computed using conservative filtering.

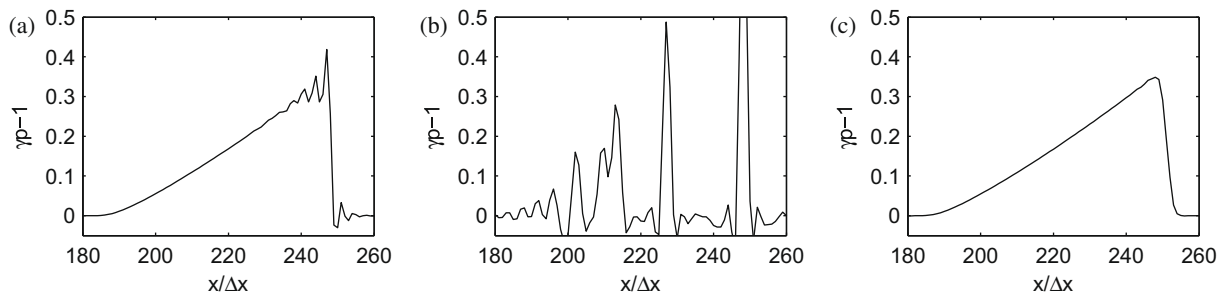


Fig. 8. Shock propagation. Pressure computed at $t = 200$ using: (a) selective filtering of the variables without shock-capturing, (b) selective filtering of the fluxes without shock-capturing, (c) selective filtering of the variables and shock-capturing based on non-conservative filtering.

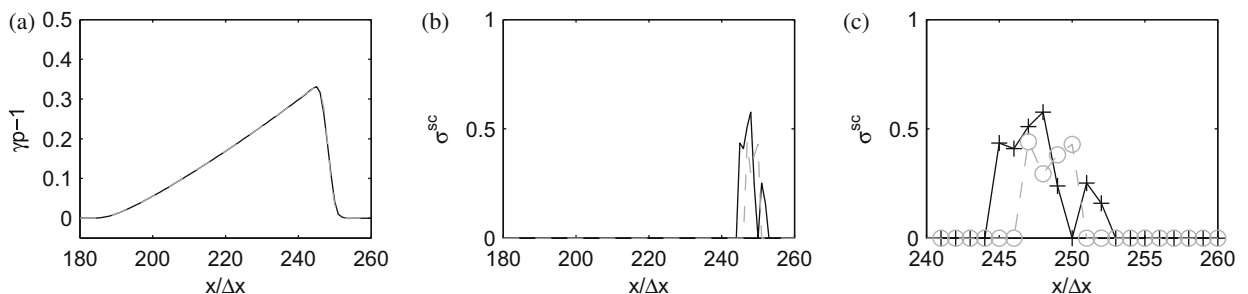


Fig. 9. Shock propagation. Influence of the shock-detection variable. Solutions computed at $t = 200$: (a) pressure, (b) and (c) magnitude σ^{sc} of the shock-capturing filtering, using filter Fo2, a threshold parameter $r_{th} = 10^{-5}$ and a shock sensor evaluated from: — pressure, - - - dilatation (+, o grid points).

Solutions calculated with a threshold value $r_{th} = 10^{-5}$ and the standard filter Fo2, using pressure or dilatation to detect the shock, are represented in Fig. 9. The two pressure profiles thus obtained do not exhibit oscillation in Fig. 9(a), and are even fairly superimposed. Estimating the shock detector from pressure or from dilatation is therefore nearly equivalent for the present problem of shock propagation. In order to find nevertheless small differences, the magnitudes of the shock-capturing filtering are plotted in Fig. 9(b) and (c). In the two cases the second-order filtering is seen to be switched on over a limited zone around the shock, containing eight points using pressure as shock-detection variable, but only four points using dilatation. Tracking the shock from dilatation rather than from pressure allows here to apply the filtering to fewer grid points.

The influence of the threshold parameter r_{th} is now investigated by displaying in Fig. 10 solutions computed using filter Fo2 and a shock detection based on dilatation, with $r_{th} = 10^{-6}$ and $r_{th} = 10^{-4}$. In Fig. 10(a), the pressure profile predicted for $r_{th} = 10^{-6}$ is smoother, whereas the profile for $r_{th} = 10^{-4}$ shows remaining, albeit of very low amplitude, Gibbs oscillations near the shock. This suggests that the shock-capturing method is more dissipative when the value of r_{th} is decreased. More precisely, the shock-capturing filtering appears to be applied over a wider region around the discontinuity, as indicated by the profiles of the filtering magnitude σ^{sc} in Fig. 10(c). This magnitude is nil everywhere except for four grid points when the threshold parameter is $r_{th} = 10^{-4}$, whereas 12 points are affected by the second-order filtering when $r_{th} = 10^{-6}$.

Finally the problem is solved using the following shock-capturing parameters: a threshold value $r_{th} = 10^{-5}$, a shock sensor based on dilatation, and the standard filter Fo2 or the optimized filter Fopt. The pressure distributions obtained in Fig. 11(a) are very similar. The optimized filter Fopt is therefore capable of properly capturing the shock. Furthermore one can note in Fig. 11(c) that the magnitude of the shock-capturing filtering is higher when filter Fopt is used rather than filter Fo2. Because filter Fopt is less dissipative than filter Fo2, it may have to be applied with a higher strength to handle the shock, this strength being determined dynamically from the solutions. Nevertheless this does seem to lead to a smoother solution. On the contrary using filter Fopt provides a sharper shock than filter Fo2 in Fig. 12. Implementing the optimized filter in the shock-capturing procedure may then be interesting to reduce spurious damping.

4.2.2. Shock-acoustic interaction

The second non-linear problem considered is the category 1 problem 2 formulated in the third CAA Workshop [44] to simulate shock-sound interaction in a transonic nozzle. To model this problem, the quasi-one-dimensional Euler equations (2) are solved over the computational domain $-10 \leq x \leq 10$, with the area of the nozzle given by

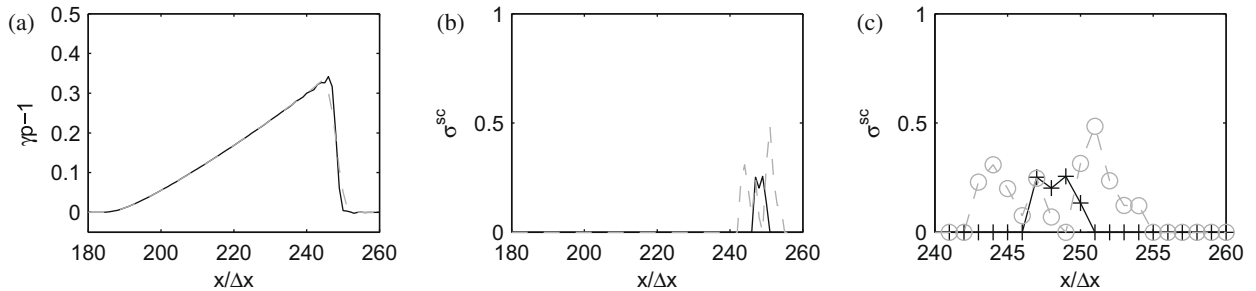


Fig. 10. Shock propagation. Influence of the threshold parameter r_{th} . Solutions computed at $t = 200$: (a) pressure, (b) and (c) magnitude σ^{sc} of the shock-capturing filtering, using filter Fo2, a shock sensor evaluated from dilatation, and: — $r_{th} = 10^{-4}$, — — $r_{th} = 10^{-6}$ (+, o grid points).

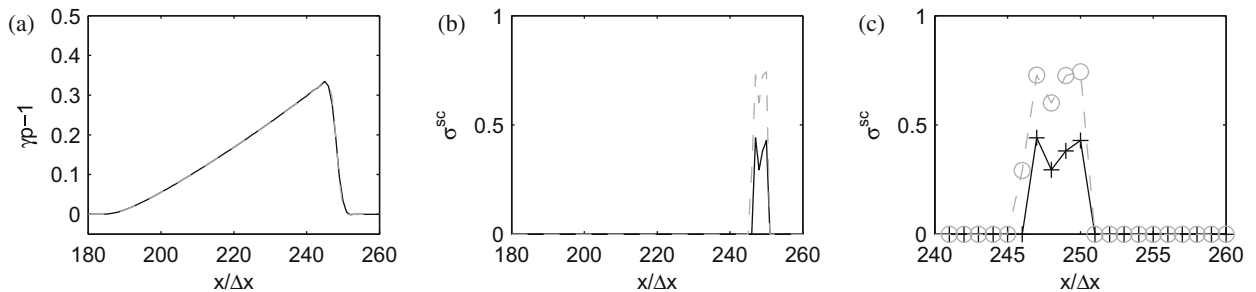


Fig. 11. Shock propagation. Influence of the shock-capturing filter. Solutions computed at $t = 200$: (a) pressure, (b) and (c) magnitude σ^{sc} of the shock-capturing filtering, using a shock sensor evaluated from dilatation, a threshold parameter $r_{th} = 10^{-5}$ and — filter Fo2, — — filter Fopt (+, o grid points).

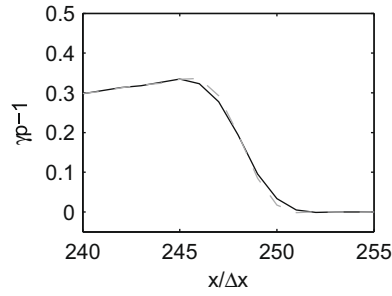


Fig. 12. Shock propagation. Influence of the shock-capturing filter. Pressure computed at $t = 200$, with the same parameters as in Fig. 11.

$$A(x) = \begin{cases} 0.536572 - 0.198086 \exp(-\ln(2)(x/0.6)^2) & \text{for } x \geq 0, \\ 1.0 - 0.661514 \exp(-\ln(2)(x/0.6)^2) & \text{for } x < 0. \end{cases}$$

At the inflow boundary, the mean pressure, velocity and pressure are specified as $\bar{p} = 1$, $\bar{u} = 0.2006533$ and $\bar{p} = 1/\gamma$. The mean pressure at the outflow boundary is set to $\bar{p} = 0.6071752$ to create a shock. Once steady state is achieved for the mean solutions, low-amplitude acoustic oscillatory disturbances are imposed at the inflow boundary for density, velocity and pressure. Their amplitudes are 10^{-5} times the mean inlet values, and their pulsation is $\omega = 0.6\pi$.

Regarding the numerical parameters, the mesh grid contains 401 points and is characterized by a constant spacing. The simulation is carried out with a CFL number of 0.8, providing a time step $\Delta t = 0.8\Delta x$. At the boundary conditions, non-linear boundary conditions based on characteristics [56] are used as in a previous reference [57]. Small correction terms have been also added in order to prevent the drift of mean inflow and outflow values. Finally, when the shock-capturing methodology is implemented, the filtering is applied in its conservative form, and the shock detector is evaluated from dilatation.

Solutions computed without shock-capturing are presented in Fig. 13. The profiles of mean density and pressure plotted in Fig. 13(a) display the presence of a shock slightly downstream of the nozzle narrowing, whose position and amplitude are found in Fig. 13(b) to be in good agreement with the analytical solution. The shock is thin and discretized by only three points, but it generates small oscillations, which are unfortunately of high amplitude with respect to the acoustic disturbances introduced at the inflow. The distribution of pressure perturbations obtained when steady state solutions are reached for the oscillatory problem thus exhibits in Fig. 13(c) strong peaks at the shock position, whereas the solutions in the upstream region containing the superposition of the incident waves and the waves reflected back at the throat, and in the downstream region where the transmitted waves are travelling compare successfully with the analytical solution [44].

The problem is then now solved using the shock-capturing methodology with a threshold value $r_{th} = 10^{-5}$, a shock detection from dilatation, and the standard filter Fo2. Mean and fluctuating solutions are represented in Fig. 14 as previously. Except at the shock position, they collapse well with the solutions determined without shock-capturing, both for the mean profiles in Fig. 14(a) and for the pressure waves in Fig. 14(c). The transmitted sound waves have in particular been affected in a negligible way by the shock-capturing method, and are in good agreement with the analytical solution [44]. This likely results from the features of the shock-detection procedure, because, as in the first non-linear problem in Section 4.2.1, the shock-capturing filtering is only applied to five points around the shock as it is indicated by the values of the filtering magnitude in Fig. 15. Using shock-capturing, the shock has moreover been smoothed so as to be discretized by 4 or 5 mesh points, but still agrees well with the analytical solution in Fig. 14(b). The strong oscillations observed in the distribution of the fluctuating pressure at the shock location without shock-capturing have also disappeared in Fig. 14(c). They have been damped by the second-order adaptive filtering.

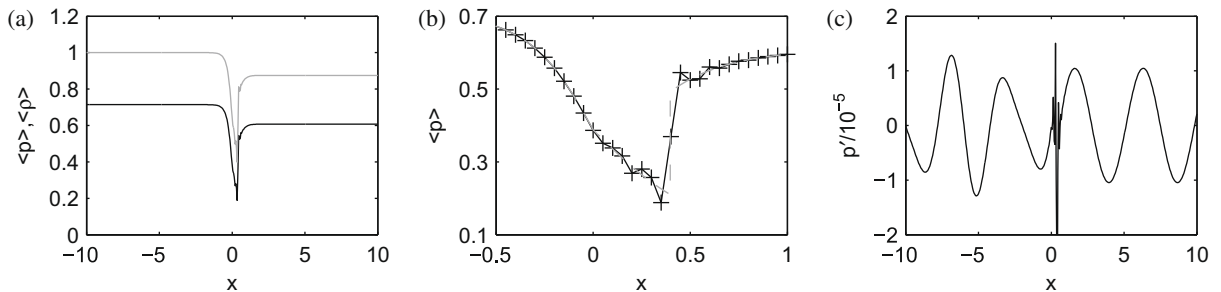


Fig. 13. Shock–acoustic interaction. Solutions computed without shock-capturing: (a) — mean pressure and — mean density, (b) — mean pressure (+ grid points) and — — corresponding analytical solution, (c) — fluctuating pressure and + corresponding analytical solution [44].

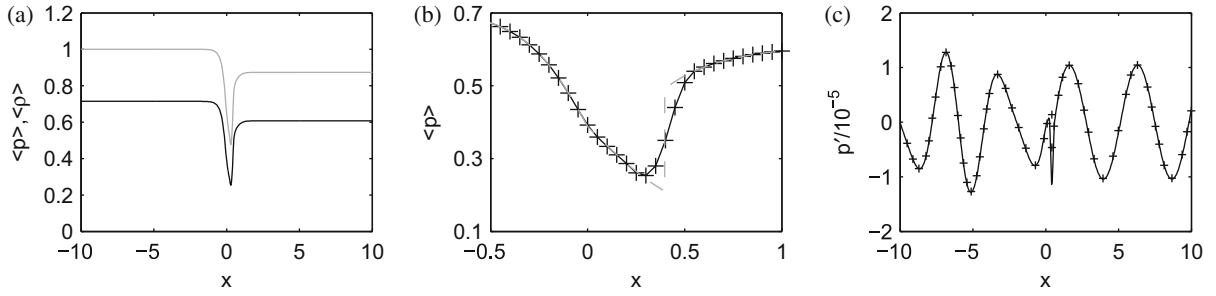


Fig. 14. Shock-acoustic interaction. Solutions computed using $r_{th} = 10^{-5}$, a shock sensor evaluated from dilatation, and filter Fo2: (a) — mean pressure and — mean density, (b) — mean pressure (+ grid points) and — — corresponding analytical solution, (c) — fluctuating pressure and + corresponding analytical solution [44].

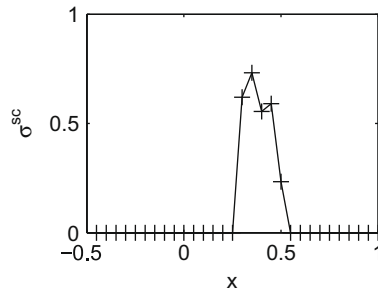


Fig. 15. Shock-acoustic interaction. Magnitude σ^{sc} of the shock-capturing filtering, using the standard second-order filter Fo2, a shock sensor evaluated from dilatation, and a threshold parameter $r_{th} = 10^{-5}$ (+ grid points).

The shock-acoustic interaction is finally simulated by implementing filter Fo_{opt} rather than filter Fo2 in the shock-capturing procedure. The results determined for the mean pressure and density, and for the fluctuating pressure are shown in Fig. 16. They collapse those obtained with filter Fo2 in Fig. 14, except at the shock location. Using the optimized filter Fo_{opt} , the shock is indeed well captured but seems sharper, the pressure gradient being discretized by 5 grid points in Fig. 16(b), which is one point less than in Fig. 14(b). The variations of fluctuating pressure around the shock also appear less attenuated in Fig. 16(c) than in Fig. 14(c).

4.2.3. Shock-tube problems

Two standard shock-tube problems, namely Sod's and Lax's problems [18,45], are now considered. They are solved from the one-dimensional Euler equations (1), and their initial conditions are

$$(\rho, u, p) = (1, 0, 0) \quad \text{for } x < 0, \quad \text{and} \quad (\rho, u, p) = (0.125, 0, 0.1) \quad \text{otherwise}$$

for the Sod test case, and

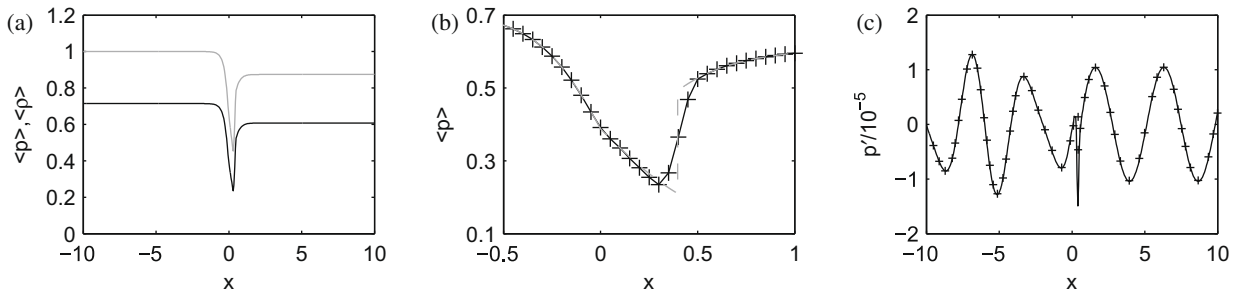


Fig. 16. Shock-acoustic interaction. Solutions computed using $r_{th} = 10^{-5}$, a shock sensor evaluated from dilatation, and filter Fo_{opt} : (a) — mean pressure and — mean density, (b) — mean pressure (+ grid points) and — — corresponding analytical solution, (c) — fluctuating pressure and + corresponding analytical solution [44].

$$(\rho, u, p) = (0.445, 0.698, 3.528) \quad \text{for } x < 0, \quad \text{and} \quad (\rho, u, p) = (0.5, 0, 0.571) \quad \text{otherwise}$$

for the Lax test case.

For the two problems, the simulations are made using a mesh grid discretizing a computational domain over $-1 \leq x \leq 1$, containing 201 points uniformly spaced. The time steps are $\Delta t = 0.25\Delta x$ for the Sod problem, and $\Delta t = 0.16\Delta x$ for the Lax problem. The shock-capturing methodology is employed with a shock detector evaluated from the dilatation, and a threshold parameter $r_{th} = 10^{-5}$, and applies the optimized filter F_{opt} in its conservative form.

The solutions obtained for density, velocity and pressure at time $t = 0.4$ for the Sod problem and at $t = 0.28$ for the Lax problem are presented in Figs. 17 and 18, respectively. In both cases, the initial conditions result in a shock wave propagating to the right, and a rarefaction wave propagating to the left from the origin. A central contact discontinuity, visible in the density distribution, is also generated. The numerical solutions show negligible Gibbs oscillations, and compare successfully with the analytical solutions derived from references [46,47]. The contact discontinuities are in particular preserved, but they appear to be slightly damped by the shock-capturing procedure. This damping occurs at the beginning of the simulations, when the shock waves and the contact discontinuities are very close to one another. Later, however, when the two fronts are well separate, the shock-capturing filtering does not apply around the linear contact discontinuities [48], because of the shock detection performed from the dilatation.

4.2.4. Shock–vortex interactions

The fourth non-linear problems examined are the interactions of a planar shock wave with a single vortex. To assess the numerical methodology, the flow conditions, namely the shock Mach number and the vortex geometry and Mach number, are first those of cases C and B, respectively computed by Inoue and Hattori [49], hereafter referred to as I&H [49], and by Inoue [50]. These authors simulated the test problem at very low Reynolds numbers using direct numerical simulation (DNS). The effects of the Reynolds number on the physical phenomena taking place during the shock–vortex interaction were found to be very small, which is also supported by good comparisons [49] between results obtained from DNS and from the Euler simulations performed by Ellzey et al. [58], for slightly different flow parameters. This led us to compute the shock–vortex problem from the 2D Euler equations (3) in the present work.

The shock wave is defined by an upstream Mach number $M_s = u_\infty/c_\infty = 1.2$, where the subscript ∞ denotes a quantity upstream of the shock and c is the sound velocity. The single vortex is assumed to be characterized by the velocity distributions of a Taylor vortex. The initial tangential and radial velocities of the vortex are expressed by

$$u_\theta(r) = M_v r \exp[(1 - r^2)/2] \quad \text{and} \quad u_r(r) = 0,$$

where the distance from the vortex core r is non-dimensionalized by the vortex radius R , and the Mach number of the vortex is $M_v = u_{\theta max}/c_\infty = 0.25$ where $u_{\theta max}$ denotes the maximum tangential velocity. The density and pressure distributions are given by

$$\rho(r) = \left[1 - \frac{\gamma - 1}{2} M_v^2 \exp(1 - r^2) \right]^{\frac{1}{\gamma - 1}} \quad \text{and} \quad p(r) = (1/\gamma)[\rho(r)]^\gamma.$$

To study the influence of the grid resolution, the problem is solved on two mesh grids with constant spacings $\Delta x = \Delta y$: a coarse grid with $\Delta x = 0.2R$ and a fine grid with $\Delta x = 0.05R$. These grids contain 651×451 and 2601×1801 points so as to both discretize a computational domain extending over $-30R \leq x \leq 100R$ and $-45R \leq y \leq 45R$. As a comparison, the grid spacing near the planar shock wave in the DNS of I&H [49] was $\Delta x = 0.0025R$. The shocks in the present calculations are therefore significantly thicker. Initially the single vortex is located at $x = -20R$ and $y = 0$, and the planar shock wave is specified at $x = 0$ by imposing density, velocity and pressure variables corresponding to the left and right states of a steady shock. Time t is normalized by R/c_∞ , and is adjusted so that the axial position of the vortex is $x = -2R$ at $t = 0$. The simulations are carried out using a CFL number of 0.6, providing a time step $\Delta t = 0.6\Delta x/c_\infty$. The shock-capturing procedure is based on a

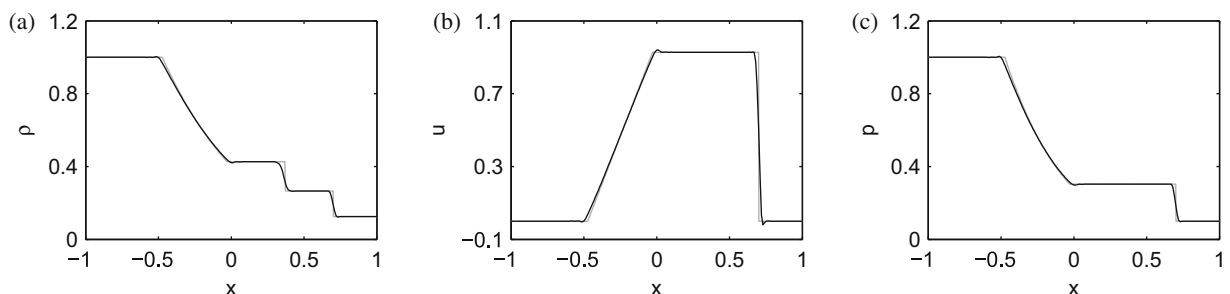


Fig. 17. Sod's shock-tube problem. — solutions computed at $t = 0.4$ using $r_{th} = 10^{-5}$, a shock sensor evaluated from dilatation, and filter F_{opt} , and — analytical solutions [46,47], for: (a) density, (b) velocity and (c) pressure.

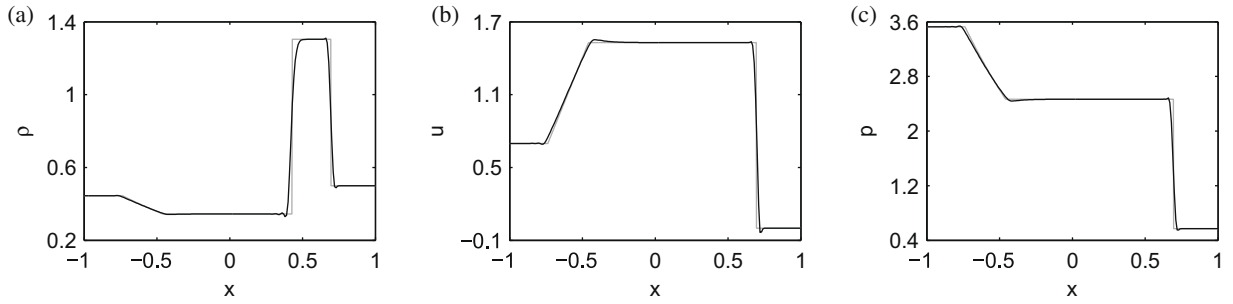


Fig. 18. Lax's shock-tube problem. — solutions computed at $t = 0.28$ using $r_{th} = 10^{-5}$, a shock sensor evaluated from dilatation, and filter Fo_{pt}, and — analytical solutions [46,47], for: (a) density, (b) velocity and (c) pressure.

shock detector calculated from dilatation, as recommended in Section 4.1.2, to avoid switching on the shock-capturing filtering in the vortex core, and on a threshold parameter set to $r_{th} = 10^{-5}$. The results shown hereafter are finally determined using the optimized filter Fo_{pt}, written in its conservative form. Similar results have been obtained using the standard filter Fo₂. The shock is however larger by one mesh size, and grid-to-grid oscillations are enhanced in this case.

Snapshots of the pressure field Δp defined by $\Delta p = (p - p_{\infty})/p_{\infty}$ upstream of the shock, and $\Delta p = (p - p_s)/p_s$ downstream, where p_{∞} and p_s are the upstream and downstream pressure values, are represented at three consecutive times in Fig. 19(a)–(c) for the coarse grid, and in Fig. 19(d)–(f) for the fine grid. No significant Gibbs oscillation is observed around the shocks, which indicates that the shocks have been correctly captured for both grids. The variation of the shock thickness with the grid resolution can also be noted at $t = 0$ in Fig. 19(a) and (c). The shock being discretized by about five points in both cases, the shock thickness is more precisely around R for the coarse grid, and $0.2R$ for the fine grid. Despite this difference, the pressure fields displayed in the top and in the bottom figures look very much alike, and also agree well with the corresponding

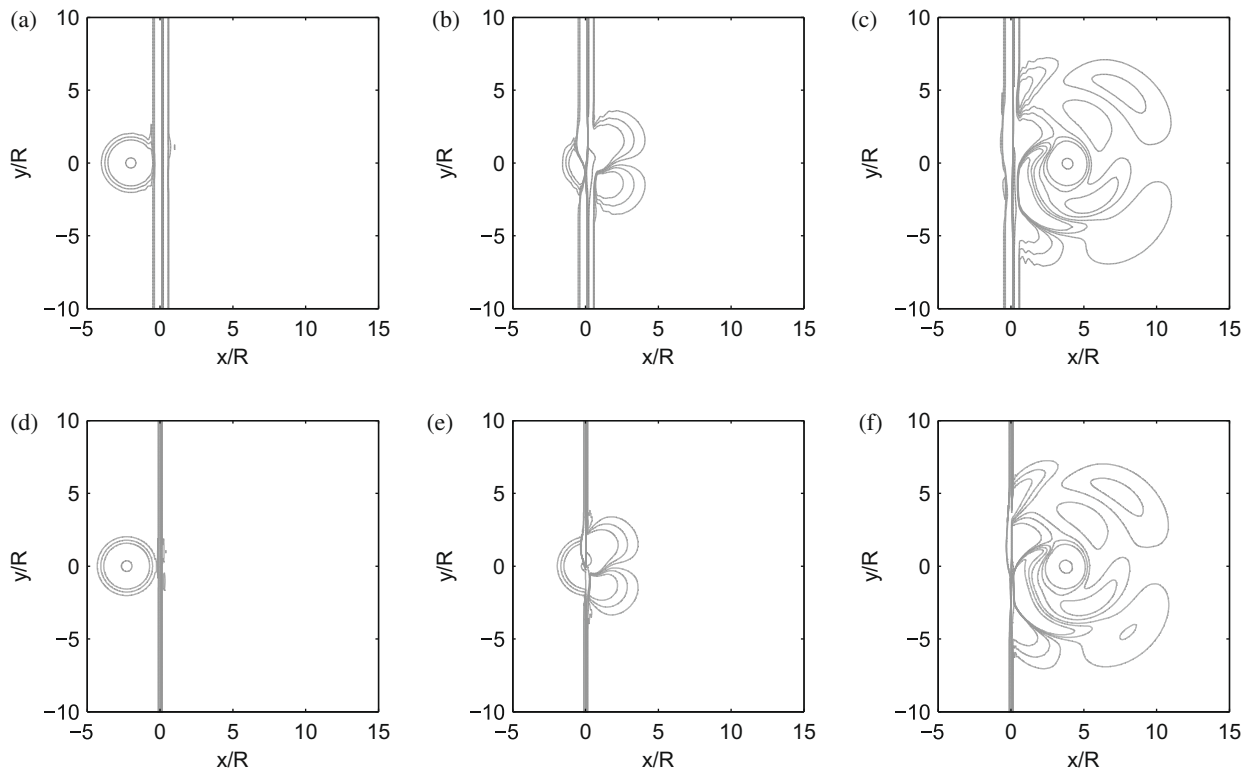


Fig. 19. Shock–vortex interaction, for shock and vortex Mach numbers $M_s = 1.2$ and $M_v = 0.25$. Representation of the contours of the pressure field $\Delta p = [-0.1, -0.01, -0.005, -0.002, -0.002, 0.005, 0.01]$, obtained with the coarse grid (top), and with the fine grid (bottom), at time: (a) and (d) $t = 0$, (b) and (e) $t = 2.04$, (c) and (f) $t = 6$. Computations performed using a shock sensor evaluated from dilatation, a threshold parameter $r_{th} = 10^{-5}$, and filter Fo_{pt}.

figures of I&H [49]. The noise generation mechanisms here are consequently nearly independent of the Reynolds number as well as of the shock size.

As the vortex interacts with the shock, the shock wave deforms, and the interactions generate sound waves in good concordance with the observations by I&H [49]. A precursor wave of quadrupolar nature is first emitted, with the clear appearance of four lobes in Fig. 19(e). The precursor wave is followed by a second sound wave, also of quadrupolar nature but of opposite sign, which can be seen in Fig. 19(c) and (f). This second sound wave results from the creation of two reflected shock waves from the incident shock, which will be shown later.

The spatial distribution of the sound pressure is investigated more quantitatively, and compared with DNS data [49,50] in Fig. 20. Profiles of pressure Δp are first plotted in Fig. 20(a) against the distance r for an angle $\theta = -45^\circ$ with respect to the downstream direction, at time $t = 10, 20$ and 30 . The profiles obtained with the coarse and the fine grids are roughly superimposed, and they agree well with the DNS curves of Inoue [50]. In particular, as the waves propagate, a pressure peak characterized by $\Delta p > 0$ corresponding to a third sound wave appears after the precursor wave and the second sound wave.

The circumferential variations of pressure Δp , associated with the precursor wave and with the second sound wave, are then represented in Fig. 20(b). The quadrupolar features of the two radiations are observed. In addition the numerical results are weakly affected by the grid resolution, and compare successfully with the DNS solutions of I&H [49]. The only notable discrepancies are noticed for angles around 180° for the second sound wave. In this case, the results might be influenced by the shock waves, depending on the shock thickness.

The way in which the shock wave deforms as the interactions with the vortex are developing is emphasized by three shadowgraphs obtained from the Laplacian of the density in Fig. 21 using the fine grid. As the initially planar shock wave passes through the vortex at time $t = 2$ in Fig. 21(a), its shape is distorted into an S-shape. For shock and vortex Mach numbers $M_s = 1.2$ and $M_v = 0.25$, the interactions are weak and a Mach reflection is then observed [59] with the formation of two reflected waves which elongate circumferentially and swirl around the vortex in Fig. 21(b), as well as two slip-lines emanating from triple points in Fig. 21(c).

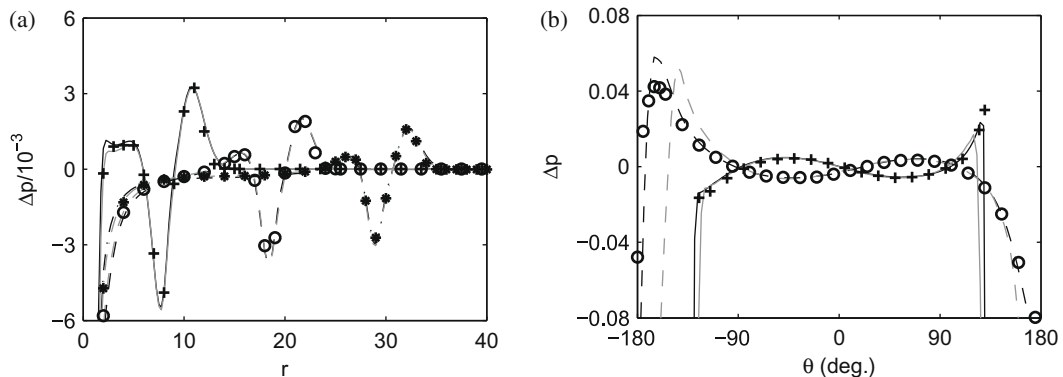


Fig. 20. Shock–vortex interaction. (a) Radial profiles of pressure Δp for $\theta = -45^\circ$ from the vortex centre, at $t = 10$: — fine grid, — coarse grid, + Inoue [50], at $t = 20$: --- fine grid, --- coarse grid, o Inoue [50], and at $t = 30$: -.-.- fine grid, -.-.- coarse grid, * Inoue [50]; (b) circumferential distributions of Δp at $t = 6$, at $r = 6.0$ (precursor): — fine grid, — coarse grid, + I&H [49], and at $r = 3.7$ (second sound): --- fine grid, --- coarse grid, I&H [49]. Same computations as in Fig. 19.

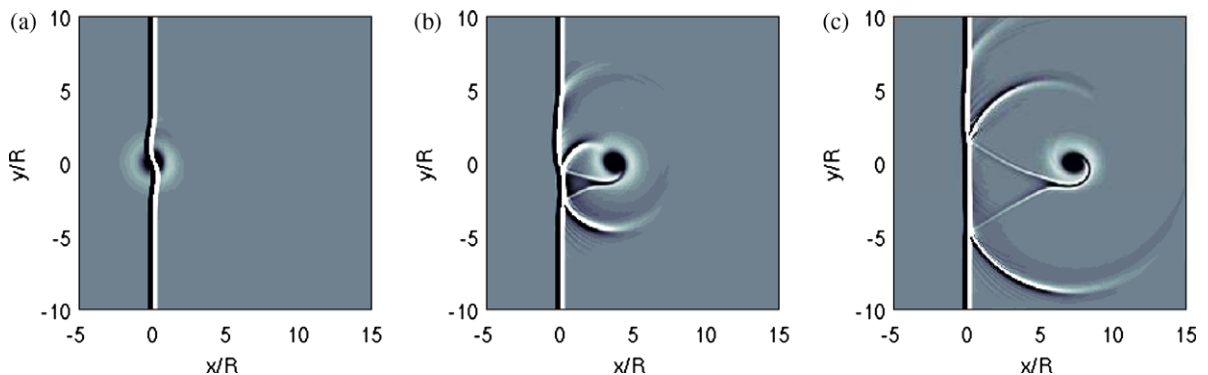


Fig. 21. Shock–vortex interaction. Representation of the shadowgraphs obtained for $\nabla^2 \rho$ with the fine grid, at time: (a) $t = 2$, (b) $t = 6$, (c) $t = 10$. Same computation as in Fig. 19.

To finally examine how the shock-capturing methodology applies when the shock wave interacts with a stronger vortex, simulations in which the vortex Mach number is changed to $M_v = 1$ whereas the shock wave Mach number as well as the computational parameters are not modified with respect to the previous calculations are performed. This shock–vortex configuration was investigated numerically by Zhang et al. [60]. Strong interactions characterized by a regular reflection pattern [59] and by multistage features [60] are expected to occur.

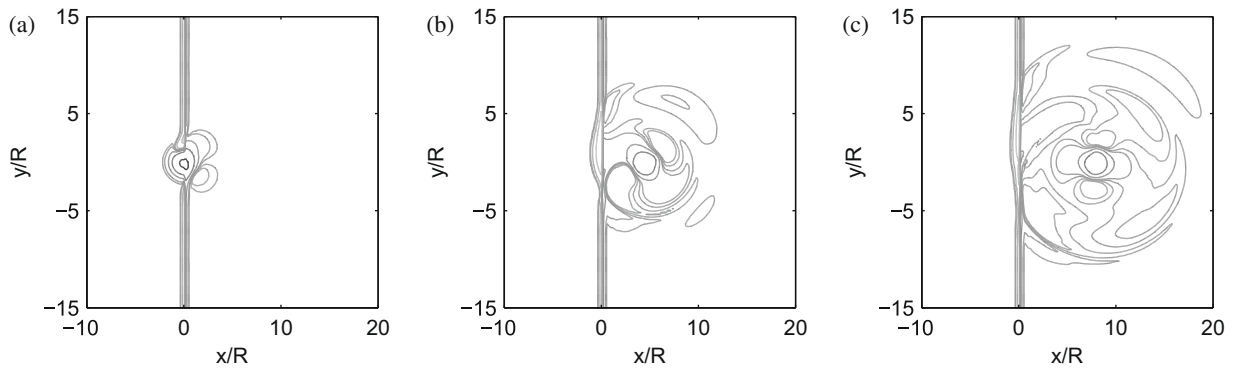


Fig. 22. Shock–vortex interaction, for shock and vortex Mach numbers $M_s = 1.2$ and $M_v = 1$. Representation of the contours of the pressure field $\Delta p = [-0.8, -0.3, -0.1, -0.025, -0.01, 0.01, 0.025, 0.1, 0.3]$, obtained for a shock wave aligned with the grid y direction, at time: (a) $t = 2$, (b) $t = 6$, (c) $t = 10$. Computations performed using a shock sensor evaluated from dilatation, a threshold parameter $r_{th} = 10^{-5}$, and filter F_{opt} .

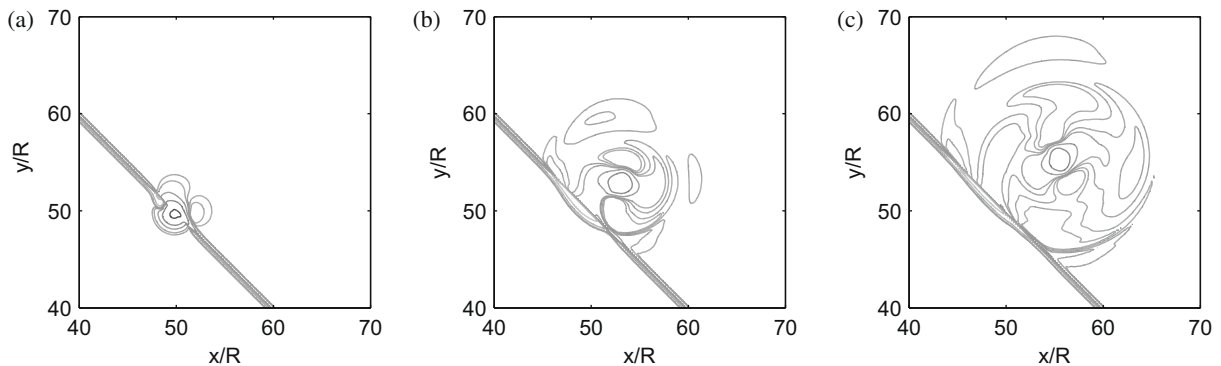


Fig. 23. Shock–vortex interaction, for shock and vortex Mach numbers $M_s = 1.2$ and $M_v = 1$. Results obtained for a shock wave making an angle of 45° relative to the grid directions. Same pressure contours and snapshot times, as well as computation parameters as in Fig. 22.

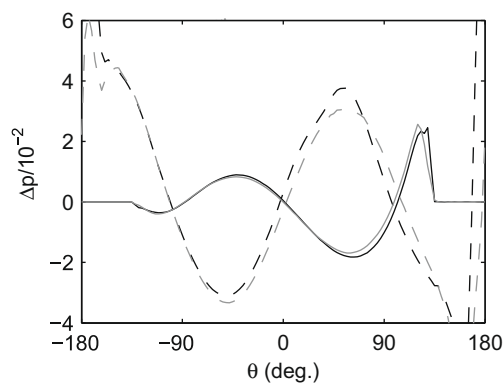


Fig. 24. Shock–vortex interaction. Circumferential distributions of pressure Δp at $t = 10$, at $r = 12$: — oblique shock wave, — — straight shock wave, and at $r = 7.8$: --- oblique shock wave, — — — straight shock wave. The angle θ is defined relative to the downstream direction. Same computations as in Figs. 22 and 23.

In the present study, the coarse grid with $\Delta x = 0.2R$ is used. The fluctuating pressure field Δp obtained for a shock wave aligned with the grid y -direction is presented in Fig. 22. The shock appears well captured, and the strong shock–vortex interactions do not visibly generate significant spurious oscillations. Moreover the pressure fields agree qualitatively very well with those calculated by Zhang et al. [60].

To have a greater correspondence with realistic problems, a shock wave making an angle of 45° relative to the grid directions is also considered as in Balsara and Shu [24] for instance. In practice the previous case has just been rotated through this angle. The fluctuating pressure obtained in this way is shown in Fig. 23. The oblique shock wave is clearly well taken into account by the shock-capturing methodology despite filterings are applied along the grid directions. Furthermore the interaction features and the pressure waves generated are just like those predicted in Fig. 22 for the straight shock.

To compare the results obtained with the straight and with the oblique shock waves, the circumferential variations of fluctuating pressure are plotted in Fig. 24 at time $t = 10$, for two distances from the vortex center, as a function of an angle defined relative to the downstream direction. The solutions obtained are very similar, even though small discrepancies can be noticed due to the application of the shock-capturing filtering on the coarse grid in different directions with respect to the planar shocks in the two simulations. The present methodology therefore seems to behave well for real 2D strongly-non-linear shock-containing problems.

5. Conclusion

In the present paper, a methodology based on a self-adaptive spatial filtering is developed to capture shocks in non-linear problems which have to be computed using low-dissipation schemes such as aeroacoustic problems. In order to assess and optimize the efficiency of the approach, both in terms of accuracy and computational cost, the different components of the shock-capturing procedure, including the shock detection from the flow variables, the determination of the filtering strength from the shock detector and the second-order filter applied around the shocks, are considered, and new formulations are proposed.

The shock-capturing methodology is implemented to perform inviscid unsteady simulations on uniform grids for standard 1D and 2D test cases, with and without embedded shocks, which results in a CPU time increase of only about ten percent. The results obtained show that the methodology is capable of properly smoothing shocks, without providing significant spurious dissipation. Thanks to the methods used for the shock detection and for the specification of the shock-capturing filtering strength, the adaptive filtering does not indeed apply for linear sound waves, as well as for vortical disturbances when the shock detector is evaluated from dilatation rather than from pressure as usually done. Around a shock, the filtering is moreover switched on over a very limited region containing about five points, centered on the discontinuity.

One original feature of the present methodology is that there is no arbitrary constant except for a threshold parameter r_{th} defined between 10^{-6} and 10^{-4} so that the shock-capturing filtering is turned off when the shock detector is smaller than its value. From the results obtained for the test cases, a threshold value $r_{th} = 10^{-5}$ can however be recommended, a higher value allowing to minimize the spurious dissipation whereas a lower value leads to damp shocks more strongly. In order to handle shocks in an appropriate way, it also appears necessary to apply a filtering of second-order, in a conservative form. The standard second-order filter can be adopted, but another second-order filter displaying optimized characteristics in the Fourier space is proposed. This new filter is successfully used to compute flows embedding shocks, yielding improved results with respect to the standard second-order filter.

Finally, the feasibility of dealing with CAA problems using the shock-capturing methodology is demonstrated by simulating the building-block problem of 2D weak and strong interactions between a shock and a vortex. The unsteady phenomena taking place in this problem, specially regarding noise generation, are accurately reproduced. Further 2D and 3D studies are now certainly required to assess the relevance of the present methodology for more complex flow configurations. It will be for instance employed for carrying out direct noise computations for realistic shock-containing flows such as supersonic jets.

Acknowledgments

A part of this work was done in the framework of the “Noise Generation in Turbulent Flows” project initiated by DFG/CNRS. The second author is grateful to the Centre National d’Etudes Spatiales (CNES) for financial support. The authors would like to thank also Roberto Della Ratta Rinaldi for his works during his Master training at Ecole Centrale de Lyon. Computations were performed on the Nec-SX8 at the Institut du Développement et des Ressources en Informatique Scientifique (IDRIS-CNRS).

References

- [1] C.K.W. Tam, Computational aeroacoustics: issues and methods, *AIAA J.* 33 (10) (1995) 1788–1796.
- [2] T. Colonius, S.K. Lele, Computational aeroacoustics: progress on nonlinear problems of sound generation, *Prog. Aerospace Sci.* 40 (2004) 345–416.
- [3] S.K. Lele, Compact finite difference schemes with spectral-like resolution, *J. Comput. Phys.* 103 (1) (1992) 16–42.
- [4] C.K.W. Tam, J.C. Webb, Z. Dong, A study of the short wave components in computation acoustics, *J. Comput. Acoust.* 1 (1) (1993) 1–30.
- [5] C.K.W. Tam, H. Shen, Direct computation of nonlinear acoustic pulses using high order finite difference schemes, *AIAA-93-4325*. 1993.
- [6] M.R. Visbal, D.V. Gaitonde, High-order-accurate methods for complex unsteady subsonic flows, *AIAA J.* 37 (10) (1999) 1231–1239.
- [7] C. Bogey, C. Bailly, A family of low dispersive and low dissipative explicit schemes for flow and noise computations, *J. Comput. Phys.* 194 (1) (2004) 194–214.
- [8] C. Bogey, C. Bailly, Contributions of CAA to jet noise research and prediction, *Int. J. Comput. Fluid Dynam.* 18 (6) (2004) 481–491.

- [9] M. Wang, J.B. Freund, S.K. Lele, Computational prediction of flow-generated sound, *Annu. Rev. Fluid Mech.* 38 (2006) 483–512.
- [10] D.P. Rizzetta, M.R. Visbal, G.A. Blaisdell, A time-implicit high-order compact differencing and filtering scheme for large-eddy simulation, *Int. J. Numer. Methods Fluids* 42 (6) (2003) 665–693.
- [11] C. Bogey, C. Bailly, Large eddy simulations of transitional round jets: influence of the Reynolds number on flow development and energy dissipation, *Phys. Fluids* 18 (6) (2006) 065101.
- [12] J. Berland, C. Bogey, C. Bailly, Numerical study of screech generation in a planar supersonic jet, *Phys. Fluids* 19 (2007) 075105. 1–14.
- [13] A. Harten, High resolution schemes for hyperbolic conservation laws, *J. Comput. Phys.* 49 (1983) 357–393.
- [14] A. Harten, B. Engquist, S. Osher, S.R. Chakravarthy, Uniformly high order accurate essentially non-oscillatory schemes III, *J. Comput. Phys.* 71 (2) (1987) 231–303.
- [15] H.C. Yee, Construction of explicit and implicit symmetric TVD schemes and their applications, *J. Comput. Phys.* 68 (1987) 151–179.
- [16] C. Shu, S. Osher, Efficient implementation of essentially non-oscillatory shock-capturing schemes, *J. Comput. Phys.* 77 (1988) 439471.
- [17] C. Shu, S. Osher, Efficient implementation of essentially non-oscillatory shock-capturing schemes, II, *J. Comput. Phys.* 83 (1989) 3278.
- [18] G.-S. Jiang, C.-W. Shu, Efficient implementation of weighted ENO schemes, *J. Comput. Phys.* 126 (1) (1996) 202–228.
- [19] C.-W. Shu, Essentially non-oscillatory and weighted essentially non-oscillatory schemes for hyperbolic conservation laws, NASA/CR-97-206253, NASA ICASE Report No. 97-65, 1997.
- [20] S. Pirozzoli, CAA for flow/acoustic interaction and high speed flows with shocks, in VKI Lecture Series 2005–2006, Von Karman Institute for Fluid Mechanics.
- [21] R. Hannappel, T. Hauser, R. Friedrich, A comparison of ENO and TVD schemes for the computation of shock-turbulence interaction, *J. Comput. Phys.* 121 (1) (1995) 176–184.
- [22] E. Garnier, M. Mossi, P. Sagaut, P. Comte, M. Deville, On the use of shock-capturing schemes for large-eddy simulations, *J. Comput. Phys.* 153 (1999) 273–311.
- [23] M. Arora, P.L. Roe, A well-behaved TVD limiter for high-resolution calculations of unsteady flows, *J. Comput. Phys.* 132 (1997) 3–11.
- [24] D.S. Balsara, C.-W. Shu, Monotonicity preserving weighted essentially non-oscillatory schemes with increasingly high order of accuracy, *J. Comput. Phys.* 160 (2) (2000) 405–452.
- [25] S. Pirozzoli, On the spectral properties of shock-capturing schemes, *J. Comput. Phys.* 219 (2006) 489–497.
- [26] V. Daru, X. Gloerfelt, Aeroacoustic computations using a high-order shock-capturing scheme, *AIAA J.* 45 (10) (2007) 2474–2486.
- [27] S.A. Karabazov, V.M. Goloviznin, New efficient high-resolution method for nonlinear problems in aeroacoustics, *AIAA J.* 45 (12) (2007) 2861–2871.
- [28] N.A. Adams, K. Shariff, A high-resolution hybrid compact-ENO scheme for shock-turbulence interaction problems, *J. Comput. Phys.* 127 (1) (1996) 27–51.
- [29] H.C. Yee, N.D. Sandham, M.J. Djomehri, Low-dissipative high-order shock-capturing methods using characteristic-based filters, *J. Comput. Phys.* 150 (1999) 199–238.
- [30] S. Pirozzoli, Conservative hybrid compact-WENO schemes for shock-turbulence interaction, *J. Comput. Phys.* 178 (2002) 81–117.
- [31] M.R. Visbal, D.V. Gaitonde, Shock capturing using compact-differencing-based methods, AIAA-2005-1265, 2005.
- [32] A. Jameson, W. Schmidt, E. Turkel, Numerical solutions of the Euler equations by finite volume methods using Runge–Kutta time-stepping schemes, AIAA-81-1259, 1981.
- [33] T.H. Pulliam, Artificial dissipation models for the Euler equations, *AIAA J.* 24 (12) (1986) 1931–1940.
- [34] R.C. Swanson, E. Turkel, On central-difference and upwind schemes, *J. Comput. Phys.* 101 (1992) 292–306.
- [35] D.P. Lockard, P.J. Morris, Radiated noise from airfoils in realistic mean flows, *AIAA J.* 36 (6) (1998) 907–914.
- [36] J.W. Kim, D.J. Lee, Adaptive nonlinear artificial dissipation model for computational aeroacoustics, *AIAA J.* 39 (5) (2001) 810–818.
- [37] R. Hixon, D. Bhate, M. Nallasamy, S. Sawyer, Shock-capturing dissipation schemes for high-accuracy, Computational AeroAcoustics (CAA) codes, AIAA-2006-2413, 2006.
- [38] T. Emmert, P. Lafon, C. Bailly, Computation of aeroacoustic phenomena in subsonic and transonic ducted flows, AIAA-2007-3429, 2007.
- [39] P.I. Crumpton, G.J. Shaw, A vertex-centred finite volume method with shock detection, *Int. J. Numer. Methods Fluids* 18 (1994) 605–625.
- [40] S.-C. Lo, G.A. Blaisdell, A.S. Lyrintzis, High-order shock capturing schemes for turbulence calculations, AIAA-2007-827, 2007.
- [41] F. Ducros, V. Ferrand, F. Nicoud, C. Weber, D. Darracq, C. Gacherieu, T. Poinso, Large-eddy simulation of the shock/turbulence interaction, *J. Comput. Phys.* 152 (2) (1999) 517–549.
- [42] E. Garnier, P. Sagaut, M. Deville, A class of explicit ENO filters with application to unsteady flows, *J. Comput. Phys.* 170 (2001) 184–204.
- [43] C.K.W. Tam, Benchmark problems and solutions, ICASE/LaRC Workshop on Benchmark Problems in Computational Aeroacoustics, NASA CP 3300, 1995, pp. 1–13.
- [44] R. Hixon, J. Wright, Solution of category 1 problem 2, Third ICASE/LaRC Workshop on Benchmark Problems in Computational Aeroacoustics, NASA CP 2000-209790, 2000, pp. 33–40.
- [45] G.A. Sod, A survey of several finite difference methods for systems of nonlinear hyperbolic conservation law, *J. Comput. Phys.* 27 (1) (1978) 1–31.
- [46] C. Hirsh, Numerical Computation of Internal and External Flows, Computational Methods for Inviscid and Viscous Flows, vol. 2, Wiley-Interscience, Chichester, 1990.
- [47] G.B. Whitham, Linear and Nonlinear Waves, Wiley, New York, 1974.
- [48] R.J. LeVeque, Finite Volume Methods for Hyperbolic Problems, Cambridge University Press, Cambridge, 2002.
- [49] O. Inoue, Y. Hattori, Sound generation by shock–vortex interactions, *J. Fluid Mech.* 380 (1999) 81–116.
- [50] O. Inoue, Propagation of sound generated by weak shock–vortex interaction, *Phys. Phys.* 12 (5) (2000) 1258–1261.
- [51] C. Bogey, C. Bailly, On the application of explicit filtering to the variables or fluxes of linear equations, *J. Comput. Phys.* 225 (2007) 1211–1217.
- [52] C. Bogey, C. Bailly, Investigation of downstream and sideline subsonic jet noise using large eddy simulations, *Theoret. Comput. Fluid Dynam.* 20 (1) (2006) 23–40.
- [53] C. Bogey, C. Bailly, An analysis of the correlations between the turbulent flow and the sound pressure fields of subsonic jets, *J. Fluid Mech.* 583 (2007) 71–97.
- [54] O. Marsden, C. Bogey, C. Bailly, Direct noise computation of the turbulent flow around a zero-incidence airfoil, *AIAA J.* 46 (4) (2008) 874–883.
- [55] C.K.W. Tam, Z. Dong, Radiation and outflow boundary conditions for direct computation of acoustic and flow disturbances in a nonuniform mean flows, *J. Comput. Acoust.* 4 (2) (1996) 175–201.
- [56] T. Poinso, S. Lele, Boundary conditions for direct simulations of compressible reacting flows, *J. Comput. Phys.* 101 (1) (1992) 104–129.
- [57] C. Bailly, Computation of generation and radiation of acoustic waves in supersonic flows, Third ICASE/LaRC Workshop on Benchmark Problems in Computational Aeroacoustics, NASA CP 2000-209790, 2000, pp. 283–294.
- [58] J.L. Ellzey, M.R. Henneke, J.M. Picone, E.S. Oran, The interaction of a shock with a vortex: shock distortion and the production of acoustic waves, *Phys. Fluids* 7 (1) (1995) 172–184.
- [59] F. Grasso, S. Pirozzoli, Shock-wave–vortex interactions: shock and vortex deformations, and sound production, *Theoret. Comput. Fluid Dynam.* 13 (6) (2000) 421–456.
- [60] S. Zhang, Y.-T. Zhang, C.-W. Shu, Multistage interaction of a shock wave and a strong vortex, *Phys. Fluids* 17 (11) (2005) 116101.